

# Toward an Ideal Polymer Binder Design for High-Capacity Battery Anodes

Mingyan Wu,<sup>†</sup> Xingcheng Xiao,<sup>‡</sup> Nenad Vukmirovic,<sup>§</sup> Shidi Xun,<sup>†</sup> Prodip K. Das,<sup>†</sup> Xiangyun Song,<sup>†</sup> Paul Olalde-Velasco,<sup>||</sup> Dongdong Wang,<sup>†</sup> Adam Z. Weber,<sup>†</sup> Lin-Wang Wang,<sup>¶</sup> Vincent S. Battaglia,<sup>†</sup> Wanli Yang,<sup>\*||</sup> and Gao Liu<sup>\*†</sup>

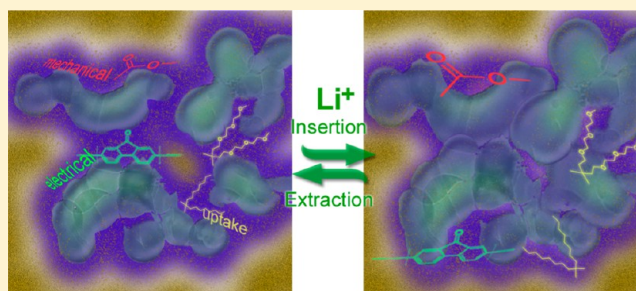
<sup>†</sup>Environmental Energy Technologies Division, <sup>||</sup>Advanced Light Source, and <sup>¶</sup>Materials Sciences Division, Lawrence Berkeley National Laboratory, Berkeley, California 94720, United States

<sup>‡</sup>Global Research & Development Center, General Motors, Warren, Michigan 48090, United States

<sup>§</sup>Scientific Computing Laboratory, Institute of Physics Belgrade, University of Belgrade, 11080 Belgrade, Serbia

## S Supporting Information

**ABSTRACT:** The dilemma of employing high-capacity battery materials and maintaining the electronic and mechanical integrity of electrodes demands novel designs of binder systems. Here, we developed a binder polymer with multifunctionality to maintain high electronic conductivity, mechanical adhesion, ductility, and electrolyte uptake. These critical properties are achieved by designing polymers with proper functional groups. Through synthesis, spectroscopy, and simulation, electronic conductivity is optimized by tailoring the key electronic state, which is not disturbed by further modifications of side chains. This fundamental allows separated optimization of the mechanical and swelling properties without detrimental effect on electronic property. Remaining electronically conductive, the enhanced polarity of the polymer greatly improves the adhesion, ductility, and more importantly, the electrolyte uptake to the levels of those available only in nonconductive binders before. We also demonstrate directly the performance of the developed conductive binder by achieving full-capacity cycling of silicon particles without using any conductive additive.



of the volume change in high-capacity electrodes have been extensively explored, such as metal alloy, Si/C composite,<sup>9,10</sup> Si wire,<sup>11,12</sup> tube,<sup>13–16</sup> and especially nanoengineering,<sup>17–19</sup> an efficient battery binder system is the ultimate solution for assembling high-capacity but severe-volume-change electrodes, and has not been developed.

A traditional binder system is dual-component based, essentially with two components for two different functionalities. Polymer binders, such as polyvinylidene fluoride (PVDF), mechanically hold the active materials and additives together. Electronically conductive additives, such as acetylene black (AB), are necessary to ensure electrical conductivity of the entire electrode. In a porous composite electrode, the nonconductive polymer binder combines with AB conductive additives to maintain the electronic connection. In addition to the mechanical adhesion and electronic connection, the polymer should swell in electrolyte to provide enough ionic conductivity. Although such classic dual-component binder design is popular in the current Li-ion batteries, it does not work well

## INTRODUCTION

Energy storage is a critical but weak link in the chain of sustainable energy applications. Developing high-capacity battery systems without sacrificing the safety, cost, power, and stability standards remains a formidable challenge, and requires optimized performance of every battery component.<sup>1,2</sup> Besides other elemental parts in batteries, such as electrodes and the electrolyte, an efficient binder is critical to maintain both the electronic and mechanical integrity of battery electrodes. An ideal battery binder should provide inexhaustible tolerance of the large volume change of high-capacity materials during battery operation. Traditional binder systems involving nonconductive polymer and conductive additives encounter technical challenges when applied in high-capacity electrodes. For example, the Li-ion alloying capacity of silicon is 4200 mAh/g to the Li<sub>22</sub>Si<sub>5</sub> phase, more than 10 times higher than that of the current graphite anode; about 3500 mAh/g is accessible during electrochemical lithiation to the Li<sub>15</sub>Si<sub>4</sub> stage.<sup>3,4</sup> However, around 300% of volume expansion was observed when Si is fully electrochemically lithiated. In a conventional binder system, this violent volume change disrupts the electrode integrity during the charge and discharge cycles.<sup>3–8</sup> Although approaches to overcome the adverse effects

Received: May 31, 2013

Published: July 15, 2013

for the high-capacity electrodes with large volume change.<sup>20–22</sup> Mechanically, high-capacity electrode materials tend to generate more than an order of magnitude higher stress in the electrode than those of graphite during lithiation. The stress disrupts the mechanical integrity, leading to electrode fracture and delamination.<sup>23</sup> More seriously, the electronic integrity of electrodes relies on the connections between the nonadhesive conductive additives and active materials. Even with extensive amounts of conductive additive, this connection will break after extended cycles of large volume change.<sup>24,25</sup>

Therefore, an ideal battery binder system for high-capacity electrodes should be able to provide: (1) inherent electronic conductivity under the Li-ion battery environment, (2) mechanical adhesion and ductility with inexhaustible tolerance of large volume change, and (3) electrolyte uptake to warrant high ionic conductivity (Figure 1). Conductive polymers with

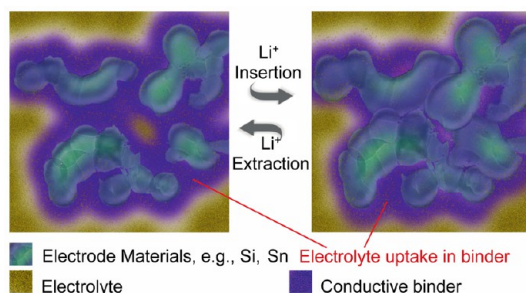


**Figure 1.** Schematic of an ideal binder system for high-capacity battery electrodes. The binder developed in this work features optimized electronic conductivity in a lithium environment, strong mechanical adhesion, ductility, and high electrolyte uptake. All these optimized functionalities were integrated into one conductive polymer.

improved adhesion to active material particles have shown potential for improving the electronic connection in Si anodes.<sup>26–29</sup> Our previous work showcased the power of utilizing advanced spectroscopy and simulation for optimizing the electronic property of conductive polymer in Li-ion battery environment. Cycling of Si with a capacity of 2100 mAh/g has been demonstrated with conductive polymer binder.<sup>30</sup> Based on the established methodology for synthetically controlling the electronic property of conductive polymers, here we report a toward ideal polymer binder system through a new conceptual design with combined chemical synthesis, quantum calculation, spectroscopic, and mechanical testing tools. The developed polymer exhibits great electronic and mechanical properties as well as enhanced electrolyte uptake, meeting all the aforementioned challenges of an ideal binder system. Full capacity (3750 mAh/g) cycling of commercial Si particles without using any conductive additive is realized through this conceptual change on the battery binder, i.e., from the traditional multicomponent to the developed single-component multifunctionality system.

## RESULTS AND DISCUSSION

### Design of Conductive Polymer As Battery Binder.

Figure 2 shows the design concept and synthesis schematic of the conductive polymer. Three types of functional groups were introduced to polyfluorene (P) type conductive polymers for optimizing the electronic, mechanical, and electrolyte-uptake properties. First, fluorenone (F) was incorporated to tailor the electronic structure of the polymer, so the polymer could be

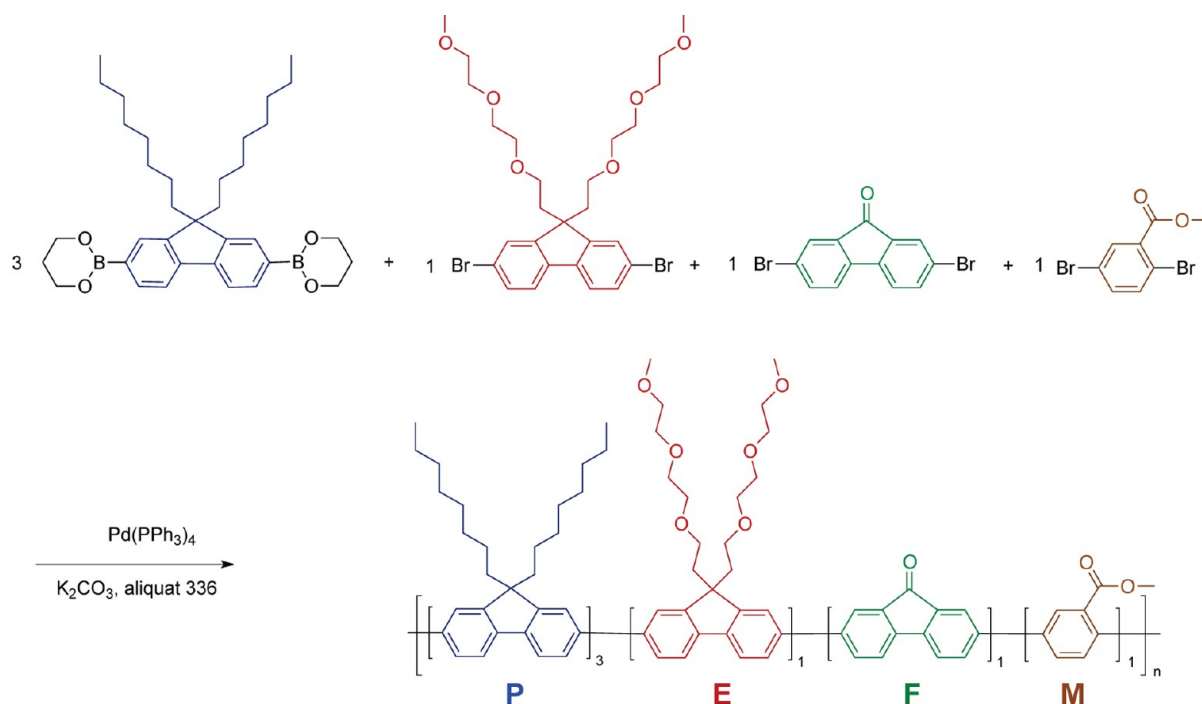
cathodically doped under the reducing lithium environment to improve its overall electric conductivity.<sup>30</sup> Second, methyl benzoate ester (M) groups were copolymerized to improve the chain flexibility of the polymer and therefore strengthen the mechanical adhesion force between the active materials and the polymer binder. Third, triethyleneoxide monomethylether (E) side chains were introduced to the conductive polymer to enhance its electrolyte uptake capability.

The challenge for designing a single-component battery binder is that modifications for improving the individual functionality should not be detrimental to each other. In our polymer system, this challenge is circumvented by modifying only the side chains on the backbone of the PF conductive polymers. Below, we first establish the fundamental that the ether side chains do not contribute to the relevant electronic states pertaining to the electronic conductivity, as justified by spectroscopy and calculations (Figure 3). Partially replacing octyl side chains with triethyleneoxide monomethylether moieties significantly enhanced the polarity of the polymers, leading to much improved electrolyte uptake (Figure 4a,b). Additionally, incorporation of the ether moiety in the polymer increased both the interface adhesion and the ductility (Figure 4c–f) to better eliminate stress-induced fracture.<sup>31–33</sup> In fact, polyethyleneoxide (PEO) is known to form stable interface layer between lithium metal and the PEO electrolyte; therefore, it is chemically suitable in the anode environments.<sup>34</sup> PF polymers with such ether side chains are thus able to maintain high levels of electronic conductivity, mechanical flexibility, and electrolyte uptake individually.

### Maintaining Key Electronic States for Optimized Electronic Properties.

We have previously shown that tailored electronic structure by introducing the F group into polyfluorene will lead to optimized electronic conductivity in a reducing lithium environment.<sup>30</sup> The binding energy of lithium to the F group (2.46 eV) is close but a bit higher than that of the Si (2.42 eV), so Li will be bonded to the polymer on the F group first. A special lowest unoccupied molecular orbital (LUMO) state derived from the F group sits lower in energy than that of the Li state (Figure 3b). The electron distribution of this particular LUMO state is extended into the polymer backbone, leading to effective in situ electron doping for improving the polymer's electronic conductivity.<sup>30</sup>

Figure 3 shows the synchrotron-based soft X-ray absorption spectroscopy (XAS) results,<sup>35</sup> collected at the Advanced Light Source (ALS), and the DFT calculated band structures, performed at the National Energy Research Scientific Computing Center (NERSC). This spectroscopy was done to screen the materials and verify that the beneficial low-energy LUMO state from the F groups is maintained in the polymers with further modifications of the side chains. XAS is a direct probe of the unoccupied states through excitations of core-level electrons to the unoccupied states. So, the lowest energy features in XAS data correspond to the LUMO states with empty core holes.<sup>36</sup> Although detailed line shape analysis of XAS is a powerful tool for revealing both the physical and chemical processes of battery materials,<sup>35</sup> the analysis here focused only on the LUMO states manifested by the absorption onsets of the spectra. The results showed clearly that a low-energy shoulder feature exists for all polymers with F groups but not for the P polymer. Modifying the side chains, E and M, only lead to spectroscopic difference at higher energies away from the LUMO states (Figure S1), thus has no effect on electronic conductivity.



### Functional Groups

**P:** Polyfluorene with octyl side chains

**E:** Fluorene with triethyleneoxide monomethyl ether side chains

**F:** Fluorenone

**M:** Methyl benzoate ester

### Functionalities

Electronic conductivity

Electrolyte uptake; Mechanical

Optimized electronic conductivity

Mechanical

**Figure 2.** Synthetic scheme and the design purpose of the functional groups incorporated in the polymer binder. Functional groups contribute specific functionalities when the polymer is used as a binder in Li-ion batteries.

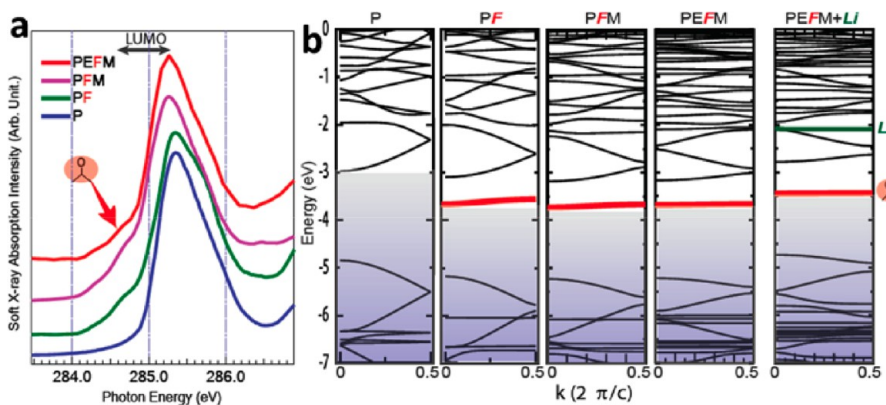


**Figure 3.** Electronic states relevant to electrical conductivity. (a) Synchrotron-based soft X-ray absorption spectra of a series of polymer binders with different chemical structures. Here we focus on low-energy onset states, which correspond to the LUMO-derived bands. All polymers with F units display a low-energy LUMO state that is about 0.7 eV below the LUMO in the P polymer. E and M functional groups only affect high-energy features (Figure S1). (b) The DFT calculation confirms all polymers with F group feature a low-energy LUMO state (red), with different high-energy states. This is consistent with the spectroscopic data. The special LUMO state (red) sits lower in energy than the Li state (green) (see Figure S2 for other polymers), leading to effective electron doping if the materials are used in lithium battery environment.

The origin of this low-energy LUMO state was confirmed by the DFT calculations (Figure 3b), which are consistent with the spectroscopic experiments. The F group derives an electron

band much lower in energy than other electron states, including the state introduced by Li (Figure S2). The calculation also confirmed the experimental evidence that adding E and M

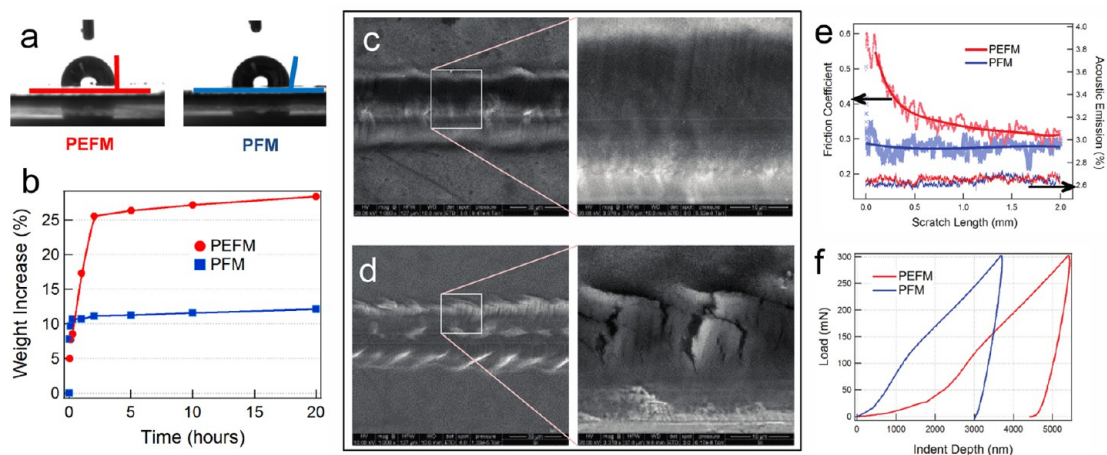


**Figure 4.** Electrolyte uptake and mechanical properties. (a) Water contact angles on the surfaces of PEFM and PFM films. The E side chains in PEFM increase the polarity and thus improve the swelling of the polymer. Therefore the PEFM has a lower contact angle with water. (b) The swelling tests of PEFM and PFM polymer film in the 1 M LiPF<sub>6</sub> EC/DEC (1:1) electrolyte. The electrolyte uptake in PEFM is three times higher than that in PFM and is at the same level as that for conventional nonconductive PVDF binder. (c,d) The scratch tests of PEFM/Si (c) and PFM/Si (d) composite electrodes. The SEM image of the scratch morphology of PEFM shows a very smooth scratch path with little crack. (e) The PEFM/Si electrode displays higher friction coefficient than that of the PFM/Si, indicating the higher binding strength of PEFM. Both have the same level of caustic emission. (f) Nanoindentation force of the PEFM is lower than the PFM at a given indentation depth. PEFM with the ether side chains shows lower modulus, thus higher ductility, than that of the PFM.

functional groups to the polymer only affects the high-energy electron states, which are not relevant to the materials' electronic conductivity. As experimentally verified in PEFM (Figure S3), and previously in the PFM polymer,<sup>30</sup> such optimized electronic structure leads to in situ electron doping of the polymers under the Li-ion chemistry, which intrinsically improves its electronic conductivity if used in lithium batteries. The electronic conductivity of polymers with F group reaches  $4.90 \times 10^{-6}$  S/cm after the first lithiation cycle. The conductivity is lower than that of AB conductive additive particles used in classic composite electrode, because the doped electrons are somewhat localized as indicated by the isosurfaces.<sup>30</sup> The specific conductivity of AB is typically in the range from 0.1 to 100 S/cm,<sup>37</sup> but both the particles and particle-to-particle connections for electron transport are rigid. AB composite tends to lose electronic conductivity entirely due to volume change of the Si materials. Therefore, such moderate improvement on conductivity of the conductive polymer binder over that of the nonconductive polymer binder has led to tremendous improvement of the Si electrode performance, as demonstrated previously in PFM polymer<sup>30</sup> and PEFM in this work.

**Electrolyte Uptake.** Li-ion transportation in the binder system is critical for achieving the full capacity of the high-capacity materials in battery electrodes, because the binder coats the surface of the active material and may impede the Li-ion diffusion. Although ion mobility in the doped conductive polymer system has been demonstrated, strategies to further improve the ion mobility are still necessary.<sup>38,39</sup> In our polymer system, this issue is tackled by improving the electrolyte uptake through the incorporation of the polar E side chains.

The enhanced polarity of the PEFM polymer results in a 3-fold electrolyte uptake (Figure 4a,b). The better swelling is due to the increased polarity of the polymer, which is indicated by the water contact angle measurements (Figure 4a). The static contact angle is 90.9° for PEFM with the E group versus 101.0° for PFM. The ether side chains tend to distribute uniformly in the polymer because they are chemically attached to the

backbone. The uniform distribution of the ether moieties in the binder helps to improve the overall electrolyte uptake. Although PFM also swells in the electrolyte solution, the total electrolyte uptake is about 10% of its final weight. In swelled PEFM films, the electrolyte uptake is tripled, accounting for 30% of the final swelling weight (Figure 4b). This number is similar to the nonconductive PVDF swelling in the electrolyte.<sup>40</sup> As explained above, the enhanced electrolyte uptake is important for allowing facile Li-ion transportation through the polymer binder to the active materials.

**Mechanical Adhesion and Ductility.** Another important benefit associated with the increased polarity of the polymer is the significantly improved adhesion force of the binder with the Si particles and with the current collector. The photo of the peel result (Figure S4) shows that almost the whole PEFM laminate persists on the current collector, while for the PFM, the delamination takes place between the electrode laminate and the current collector. This clearly shows that the large adhesion force of the PEFM binder is beyond the testing range of such conventional peeling test, which is a standard technique widely used in battery industry. Although the force to delaminate the PEFM-based laminate electrode is too strong to be measured, the great improvement on adhesion among the laminate, current collector, and particles is obvious.

The better initial adhesion in the binder system has been found to result in better cyclability and lifetime performance, although the adhesion may change as the electrolyte wets the laminates and after the electrode cycles.<sup>41,42</sup> The greatly improved binder adhesion force can be explained as follows: as the binder's polarity increases, the binder adheres with the polar silicon dioxide (SiO<sub>2</sub>) surfaces of the Si particle and the copper oxide (CuO) surface of the Cu current collector more effectively.<sup>43</sup>

In addition to the adhesion force, a compliant polymer is highly preferred for battery binder systems, because it can accommodate the stress from the active material expansion and maintain mechanical stability of electrodes. This requirement becomes critical for high-capacity electrodes because the

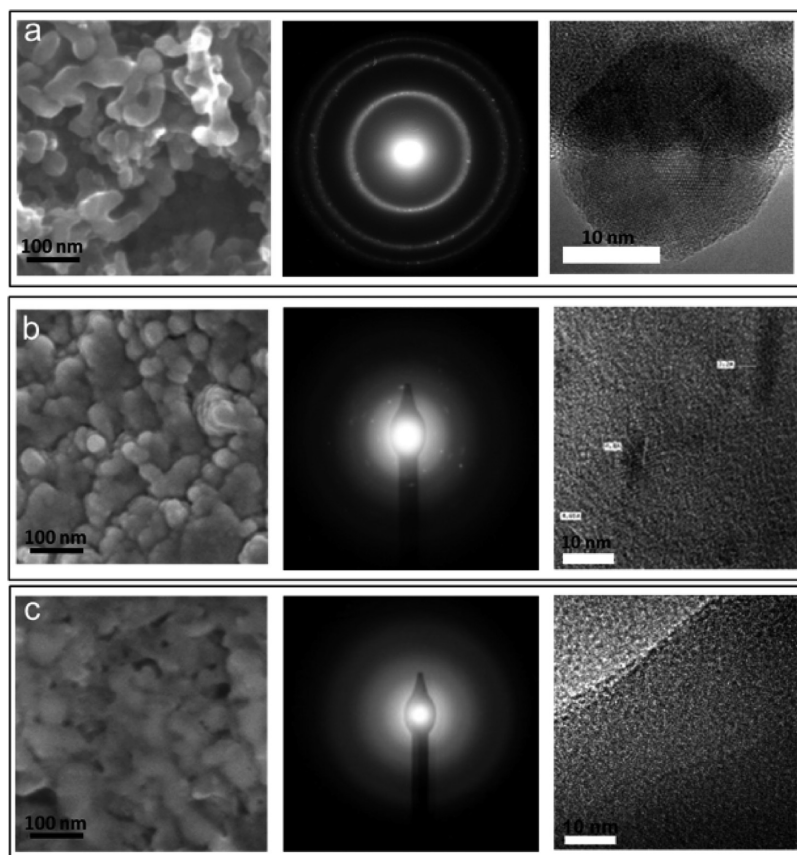


**Figure 5.** Electron microscope images polymer/Si electrodes before and after cycling. (a) SEM, electron diffraction pattern, and high-resolution TEM image of a fresh composite electrode with conductive polymer binder and Si nanoparticles. TEM was taken on a Si particle. The lattice structure of crystalline Si particles is visible. (b) Images of the PFM/Si composite electrode after one lithiation and delithiation cycle. The diffraction spots suggest the existence of crystalline Si particles. TEM confirms the existence of crystalline Si domains. (c) Images of the PEFM/Si composite electrode after one lithiation and delithiation cycle. Both the electron diffraction and TEM image indicate completely amorphous Si particle in the composite electrode.

volume expansion is at much higher scale. For example, the stress generated by Si volume expansion causes fracture of the electrode. The fracture takes place within the binder itself, and/or at the binder/Si interface, but not in the Si particles. Therefore, the issue is to address the ductility of the binder and the interfacial strength between binder and active materials.<sup>6,44</sup>

Unfortunately, most of the conductive polymers are rigid molecules that tend to have higher Young's modulus (elastic modulus) and are very brittle.<sup>45</sup> They tend to fracture under a high-stress situation. In our PEFM conductive polymer, the ether moieties are much harder to pack and assume a more random molecular configuration than that of the octyl moieties.<sup>46</sup> Therefore, incorporating a short ether moiety increases the ductility of the polymers. The more-compliant PEFM better accommodates the volume change of active materials, and they accumulate less stress in the binder and at the interface between the binder and the active materials. This improvement in molecular scale can be visualized and quantified via a scratch test and nanoindentation tests.<sup>47,48</sup> The morphology of the electrode after a scratch test between the PFM and the PEFM binder-based electrodes has shown drastic differences (Figure 4c,d). The scratch track of the PEFM electrode is very smooth, with very limited cracks of the electrode laminate. However the PFM shows major crack patterns on its scratch track. Because the scratch test simulates the stress induced by the volume change of active materials, this

result essentially demonstrates that the more compliant PEFM binder provides great tolerance of the volume change through its optimized ductility.<sup>49,50</sup>

The friction coefficient during the scratch test and nanoindentation of the composite electrode reflect the composite nature of the laminate electrode as well as the binder mechanical properties (Figure 4e-f). The friction coefficients of the two laminates are close because the composites are dominated (67%) by the active Si materials. The slightly higher friction coefficient of PEFM is consistent with the higher binding strength of PEFM with its improved adhesion, which leads to stronger interaction with the polar diamond tip used in the tests. The negligible acoustic emission indicates that the breakage of the composite takes place within the binder and/or at the interface, rather than in the Si particles, which is consistent with previous reports.<sup>6,44</sup> Since the breakage during the scratch test is not in the Si active material, the contrast on the nanoindentation results reflects the different binder properties. The obviously lower modulus of the PEFM/Si electrode is highly beneficial to enhance the tolerance of the volume change.

**Demonstration of the Toward Ideal Polymer Binder in Polymer/Si Electrodes.** Besides the comprehensive electronic and mechanical verifications, the performance of the conductive polymer binder in battery electrodes is demonstrated in this section. Because Si anodes are known to suffer the most serious

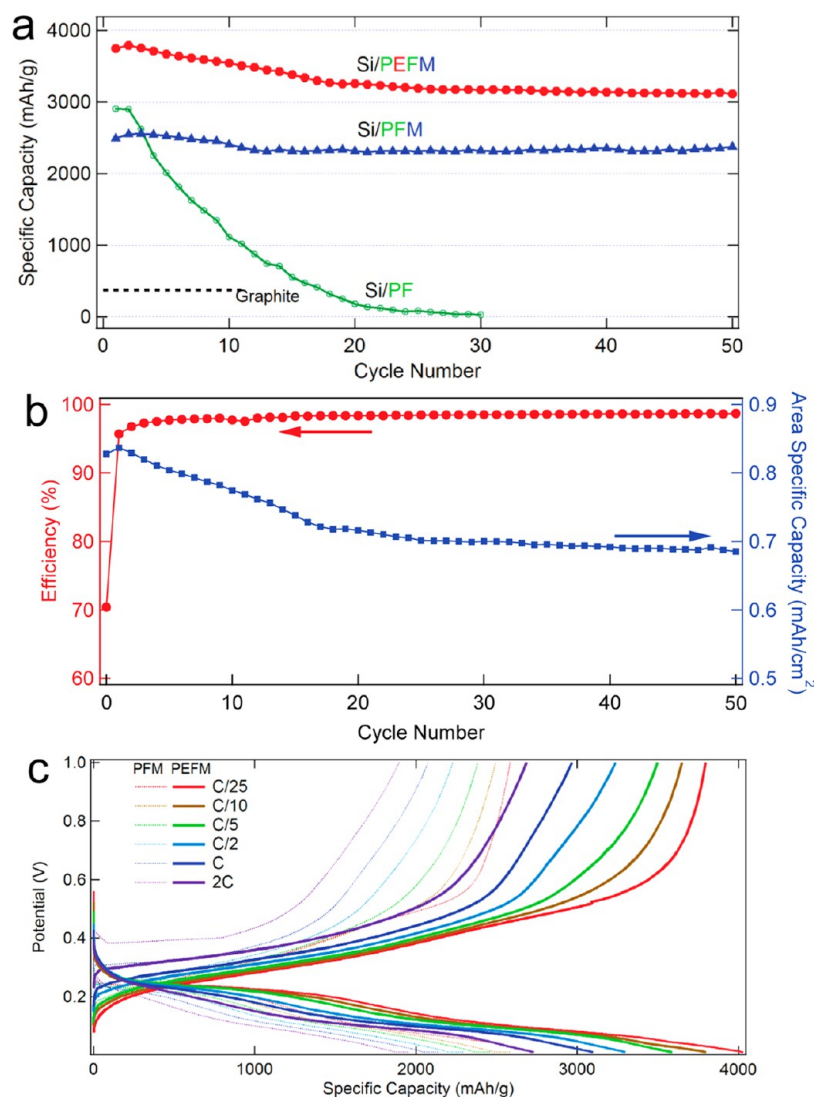


**Figure 6.** Cycling and rate performance of conductive polymer/Si electrodes without any conductive additive. (The current density at C-rate is 0.92 mAh/cm<sup>2</sup>) (a) Cycling performance of polymer/Si composite electrodes. A PEFM conductive polymer, as an ideal binder, enables the cycling with full theoretical capacity of Si at 3750 mAh/g. At this capacity, the volume change of Si is 100% higher than that of the PFM-based binder at 2500 mAh/g. (b) Coulombic efficiency and area specific capacity of the PEFM/Si electrode. (c) The rate performance of the polymer/Si electrodes with PEFM (solid) and PFM (dotted) binder. The capacity retention of Si is much higher in PEFM than that in the PFM.

volume change problem, they provide a challenging system to demonstrate the outstanding performance of our polymer binder.

To facilitate direct comparisons, electrodes were fabricated with similar Si loading of 0.22 mg/cm<sup>2</sup> and 67% of the total electrode mass, at both the PFM and PEFM base binders. The ratio of the Si to the conductive polymer binder was optimized between the Si and PFM binder in our early work, with 33% of binder showing the best performance.<sup>30</sup> The composite electrodes exhibited very similar and typical morphology (Figures 5a and S5) with polymer binder coating Si particles throughout the battery operation (Figure S6). Due to the inelasticity of the Si materials, the first lithiation converted crystalline Si into amorphous Si. For the PFM/Si electrode, Si became largely amorphous after one complete charge and discharge cycle. However, the electron diffraction image shows clear diffraction points, indicating the existence of a large number of crystalline domains, as seen in transmission electron microscopy (TEM) images (Figure 5b). The crystalline Si

domains suggest that some of the Si material did not participate in the cycling of the PFM/Si electrode. On the contrary, Si particles in the PEFM/Si electrodes were completely converted into the amorphous phase after only one cycle. This is confirmed by the completely blurred electron diffraction image as well as the high-resolution TEM image (Figure 5c).

The electron microscope images are in good agreement with the electrochemical testing data. Figure 6 shows that the cycling capacity of Si particles in the initial cycle reaches theoretical capacity (3750 mAh/g) in the PEFM/Si electrodes, indicating 100% utilization of Si material embedded in the PEFM binder. This is corresponding to 2500 mAh/g capacity of the entire laminate weight when the weight of conductive binder is included and a 1200 mAh/cm<sup>3</sup> volumetric energy density of the electrode. In both the PF/Si and PFM/Si electrodes, the delithiation capacity of Si in the first cycle is much lower. The discharge capacity and voltage plateau hold up very well in the initial cycles (Figure S7). The specific delithiation is stable and

higher in PEFM/Si than that in PFM/Si electrodes over extended cycles (Figure 6).

It is noteworthy that the electrode Si loadings are similar, so the improved gravimetric specific capacity of Si results in higher area-specific capacity of the electrode. The higher gravimetric capacity of Si materials was proportional to the higher volume expansion. The Si in the PEFM/Si has close to 100% higher volume expansion than that in the PFM/Si, but the PEFM binder effectively maintained stable capacity over the 50-cycle test. The discharge capability of the electrode at different current density was measured and compared between the two binder systems. The PEFM/Si electrode maintained the same level of rate performance with higher specific capacity. Almost full theoretical capacity was accessed at C/10 in the PEFM system. In the case of PEFM/Si where full utilization of Si is achieved, the Li needs to diffuse through the full size of the Si particles. Therefore, the Li-ion transport in the Si material itself may be limiting the rate performance, which was not a topic of this work. Additionally, the capacity decay of PEFM/Si is more than that of the PFM/Si in the first 20 cycles, which is again likely due to the Si material. Nonetheless, the 2C rate (half an hour delithiation) data still show superior specific capacity compared to the slow C/25 rate performance of the PFM/Si electrode, indicating the benefit of utilizing a PEFM conductive polymer as an ideal binder for high-capacity anodes.

## CONCLUSIONS

This work reports the design, synthesis, and testing of a toward ideal polymer binder for high-capacity battery anode systems. We successfully integrated three critical functionalities into a single-component n-type conductive polymer. Electronic, mechanical, and electrolyte-uptake properties are optimized individually without detrimental effect to each other. The electronic properties were verified through advanced theoretical and experimental techniques and demonstrated by the outstanding performance of a polymer/Si composite electrode without any conductive additive. The electrolyte uptake, adhesion, and ductility were measured through comprehensive mechanical testing experiments. Being electronic conductive, the developed PEFM polymer exhibited similar or higher levels of mechanical and swelling properties compared to non-conductive binder like PVDF. Full-capacity cycling of Si was accessed in this conductive polymer binder with excellent rate performance.

This work demonstrates that the conceptual design of a battery binder system could be based on a single-component conductive polymer with multifunctionality. Incorporating proper functional groups into a conductive polymer could reach balanced swelling and mechanical properties while maintaining the electronic conductivity. Large volume change of electrodes remains one of the major issues restricting the development of high-capacity batteries. The design concept, methodology, and practical application of a PEFM-conductive polymer are extendable for other high-capacity electrodes other than Si anodes.

## MATERIALS AND METHODS

**Raw Materials.** All the starting chemical materials for synthesis the conductive polymer were purchased from Sigma-Aldrich. Anhydrous *N*-methylpyrrolidone (NMP) with 50 ppm of water content was purchased from Aldrich Chemical Co. Silicon nanoparticles were purchased from Nanostructured & Amorphous Materials, Inc. The particle sizes were <100 nm in diameter. Li-ion electrolytes were

purchased from BASF, including 1 M LiPF<sub>6</sub> in ethylene carbonate (EC) and diethylene carbonate (DEC) (1:1 w/w), and 1 M LiPF<sub>6</sub> in DEC, and fluorinated ethylene carbonate (FEC) (7:3 w/w).

**Synthesis 2,7-Dibromo-9,9(di(oxy-2,5,8-trioxadecane))-fluorene.** 2,7-dibromofluorene (5.0 g, 15.4 mmol) was dissolved in dried THF solution (30 mL). Sodium hydride (1.0 g, 40 mmol) was added to the THF solution at room temperature and refluxed for 5 h. 10-Tosyloxy-2,5,8-trioxadecane<sup>46</sup> (11.8 g, 37 mmol) in 20 mL of dry THF was added dropwisely to the refluxed solution. The mixture was allowed to reflux overnight, then cooled down, poured into distill water, and extracted with chloroform (2 × 100 mL). The combined organic solutions were washed with saturated NaCl solution (2 × 100 mL) and distilled water (1 × 100 mL), dried over MgSO<sub>4</sub>, and concentrated under reduced pressure. Crude oil was further purified by column chromatography to provide a 5.7 g product in 60% yield. <sup>1</sup>H NMR (500 MHz, CDCl<sub>3</sub>) δ (ppm): 2.34 (t, 4H), 2.77 (t, 4H), 3.10–3.60 (m, 22H), 7.40–7.60 (m, 6H).

**Synthesis Poly(2,7-9,9-dioctylfluorene-co-2,7-9,9-(di(oxy-2,5,8-trioxadecane))fluorene-co-2,7-fluorenone-co-2,5-1-methylbenzoate ester) (PEFM).** A mixture of 9,9-dioctylfluorene-2,7-diboronic acid bis(1,3-propanediol) ester (1.10 g, 1.97 mmol), 9,9-(di(oxy-2,5,8-trioxadecane))fluorine (0.44 g, 0.71 mmol), 2,7-dibromo-9-fluorenone (0.24 g, 0.72 mmol), methyl 2,5-dibromobenzoate (0.21 g, 0.72 mmol), (PPh<sub>3</sub>)<sub>4</sub>Pd(0) (0.082 g, 0.072 mmol), and several drops of Aliquat 336 in a mixture of 13 mL of THF and 5 mL of 2 M Na<sub>2</sub>CO<sub>3</sub> solution was refluxed with vigorous stirring for 72 h under an argon atmosphere. After the reaction stopped, the solution was concentrated by vacuum evaporation, and the polymer was precipitated from methanol. The resulting polymer was further purified by precipitating from methanol twice. The final polymer was collected by suction filtration and dried under vacuum. <sup>1</sup>H NMR (500 MHz, CDCl<sub>3</sub>) δ (ppm): 8.17 (s, Ar-H), 8.07 (s, Ar-H), 7.87 (m, Ar-H), 7.68 (m, Ar-H), 7.38–7.43 (d, Ar-H), 3.67 (s, OCH<sub>3</sub>), 2.60–3.50 (m, –OCH<sub>2</sub>CH<sub>2</sub>O–), 2.10 (br, CH<sub>2</sub>), 1.72 (br, CH<sub>2</sub>), 1.17 (m, CH<sub>2</sub>), 0.80–0.90 (m, CH<sub>2</sub>, CH<sub>3</sub>). GPC (THF, PS standard): M<sub>n</sub> = 34 000, PDI = 2.3

**X-ray Absorption Spectroscopy.** Synchrotron-based carbon-K XAS spectra were collected at beamline 8.0.1 of the Advanced Light Source at LBNL. The undulator and spherical grating monochromator supply a linearly polarized photon beam with resolving power up to 6000. Polymers were spin coated on clean gold (Au) surfaces then loaded into an experimental chamber with base pressure of about 8 × 10<sup>−10</sup> Torr. To avoid artificial effects from radiation damage, experiments were done at 85 K temperature with a deliberately defocused and low-flux X-ray beam. All the samples have been measured multiple times with different flux and scan period and on different spots. Data have been carefully checked to make sure they are free of radiation damage effect. The XAS spectra shown here were collected in the total electron yield mode by registering the sample current normalized to the photon flux, which was measured simultaneously by the photocurrent of a clean Au mesh. The experimental resolution of the shown XAS spectra is better than 0.1 eV. All spectra plotted here were collected in one experiment with all samples mounted on the same holder to guarantee that the relative shift of the LUMO level is reliable.

**Quantum Chemistry Calculations.** The calculations were performed at the National Energy Research Scientific Computing Center (NERSC) facility. Electronic structure of the polymers and Li binding energies to the polymers were calculated using density functional theory (DFT) in local density approximation (LDA), as implemented in the VASP code.<sup>51</sup> The projector augmented wave method was used for the pseudopotentials.<sup>52</sup> A 400 eV plane wave cutoff was used, and the atomic relaxation was stopped when the atomic forces are smaller than 10<sup>−2</sup> eV Å<sup>−1</sup>. The *k* value in Figure 3 is along the polymer chain direction, with *c* as the period length. Absolute energy values are relative to vacuum level, which was set at zero energy.

**Microscratch and Nanoindentation.** The scratch tests were performed on a CSM nano/micro scratch tester. A constant load of 30 mN was applied during the test using a Vickers indenter with the

radius of 20 nm. The scratch length was 2 mm, and the speed was 1 mm/min.

## ■ ASSOCIATED CONTENT

### 📄 Supporting Information

Experimental details and Figures S1–S8. This material is available free of charge via the Internet at <http://pubs.acs.org>.

## ■ AUTHOR INFORMATION

### Corresponding Author

WLYang@lbl.gov; GLiu@lbl.gov

### Notes

The authors declare no competing financial interest.

## ■ ACKNOWLEDGMENTS

This work is funded by the Assistant Secretary for Energy Efficiency, Office of Vehicle Technologies of the U.S. Department of Energy, under the Batteries for Advanced Transportation Technologies (BATT) Program and by University of California, Office of the President through the University of California Discovery Grant. Soft X-ray spectroscopy was performed at the Advanced Light Source (ALS). Calculations used resources of the National Energy Research Scientific Computing Center (NERSC). NMR measurements were performed at the Molecular Foundry. Electron microscopy experiments were conducted at the National Center for Electron Microscopy (NCEM). All four facilities are located at Lawrence Berkeley National Laboratory (LBNL) and are supported by the Director, Office of Science, Office of Basic Energy Sciences, of the U.S. Department of Energy under contract no. DE-AC02-05CH11231. N.V. is supported by European Community FP7 Marie Curie Career Integration Grant (ELECTROMAT) and Serbian Ministry of Science (project ON171017).

## ■ REFERENCES

- (1) Armand, M.; Tarascon, J. M. *Nature* **2008**, *451*, 652.
- (2) Thackeray, M. M.; Wolverton, C.; Isaacs, E. D. *Energy Environ. Sci.* **2012**, *5*, 7854.
- (3) Li, J.; Dahn, J. R. *J. Electrochem. Soc.* **2007**, *154*, A156.
- (4) Boukamp, B. A.; Lesh, G. C.; Huggins, R. A. *J. Electrochem. Soc.* **1981**, *128*, 725.
- (5) Renganathan, S.; Sikha, G.; Santhanagopalan, S.; White, R. E. *J. Electrochem. Soc.* **2010**, *157*, A155.
- (6) Christensen, J.; Newman, J. *J. Solid State Electrochem.* **2006**, *10*, 293.
- (7) Hatchard, T. D.; Dahn, J. R. *J. Electrochem. Soc.* **2004**, *151*, A838.
- (8) Beattie, S. D.; Larcher, D.; Morcrette, M.; Simon, B.; Tarascon, J. M. *J. Electrochem. Soc.* **2008**, *155*, A158.
- (9) Wang, J.; Du, N.; Zhang, H.; Yu, J.; Yang, D. *J. Mater. Chem.* **2012**, *22*, 1511.
- (10) Magasinski, A.; Dixon, P.; Hertzberg, B.; Kvit, A.; Ayala, J.; Yushin, G. *Nat. Mater.* **2010**, *9*, 353.
- (11) Ge, M.; Rong, J.; Fang, X.; Zhou, C. *Nano Lett.* **2012**, *12*, 2318.
- (12) Chan, C. K.; Peng, H.; Liu, G.; McIlwrath, K.; Zhang, X. F.; Huggins, R. A.; Cui, Y. *Nat. Nanotechnol.* **2008**, *3*, 31.
- (13) Wu, H.; Chan, G.; Choi, J. W.; Ryu, I.; Yao, Y.; McDowell, M. T.; Lee, S. W.; Jackson, A.; Yang, Y.; Hu, L.; Cui, Y. *Nat. Nanotechnol.* **2012**, *7*, 309.
- (14) Song, T.; Cheng, H.; Choi, H.; Lee, J.-H.; Han, H.; Lee, D. H.; Yoo, D. S.; Kwon, M.-S.; Choi, J.-M.; Doo, S. G.; Chang, H.; Xiao, J.; Huang, Y.; Park, W. I.; Chung, Y.-C.; Kim, H.; Rogers, J. A.; Paik, U. *ACS Nano* **2012**, *6*, 303.
- (15) Song, T.; Xia, J.; Lee, J.-H.; Lee, D. H.; Kwon, M.-S.; Choi, J.-M.; Wu, J.; Doo, S. K.; Chang, H.; Il Park, W.; Zang, D. S.; Kim, H.; Huang, Y.; Hwang, K.-C.; Rogers, J. A.; Paik, U. *Nano Lett.* **2010**, *10*, 1710.
- (16) Park, M.-H.; Kim, M. G.; Joo, J.; Kim, K.; Kim, J.; Ahn, S.; Cui, Y.; Cho, J. *Nano Lett.* **2009**, *9*, 3844.
- (17) Jeong, J. H.; Jung, D. W.; Kong, B. S.; Lee, J.; Oh, E. S. *J. Ceram. Process. Res.* **2011**, *12*, S105.
- (18) Ma, H.; Cheng, F.; Chen, J.; Zhao, J.; Li, C.; Tao, Z.; Liang, J. *Adv. Mater.* **2007**, *19*, 4067.
- (19) Liu, N.; Wu, H.; McDowell, M. T.; Yao, Y.; Wang, C.; Cui, Y. *Nano Lett.* **2012**, *12*, 3315.
- (20) Cui, L.-F.; Hu, L.; Wu, H.; Choi, J. W.; Cui, Y. *J. Electrochem. Soc.* **2011**, *158*, A592.
- (21) Kasavajjula, U.; Wang, C.; Appleby, A. J. *J. Power Sources* **2007**, *163*, 1003.
- (22) Winter, M.; Besenhard, J. O. *Electrochim. Acta* **1999**, *45*, 31.
- (23) Ryu, J. H.; Kim, J. W.; Sung, Y. E.; Oh, S. M. *Electrochem. Solid State* **2004**, *7*, A306.
- (24) Zhang, W.-J. *J. Power Sources* **2011**, *196*, 13.
- (25) Park, C.-M.; Kim, J.-H.; Kim, H.; Sohn, H.-J. *Chem. Soc. Rev.* **2010**, *39*, 3115.
- (26) Koo, B.; Kim, H.; Cho, Y.; Lee, K. T.; Choi, N.-S.; Cho, J. *Angew. Chem., Int. Ed.* **2012**, *51*, 8762.
- (27) Joyce, C.; Trahey, L.; Bauer, S. A.; Dogan, F.; Vaughey, J. T. *J. Electrochem. Soc.* **2012**, *159*, A909.
- (28) Guo, J.; Wang, C. *Chem. Commun.* **2010**, *46*, 1428.
- (29) Wu, H.; Yu, G.; Pan, L.; Liu, N.; McDowell, M. T.; Bao, Z.; Cui, Y. *Nat. Commun.* **2013**, *4*, 6.
- (30) Liu, G.; Xun, S.; Vukmirovic, N.; Song, X.; Olalde-Velasco, P.; Zheng, H.; Battaglia, V. S.; Wang, L.; Yang, W. *Adv. Mater.* **2011**, *23*, 4679.
- (31) Chen, L.; Xie, X.; Xie, J.; Wang, K.; Yang, J. *J. Appl. Electrochem.* **2006**, *36*, 1099.
- (32) Chen, Z. H.; Christensen, L.; Dahn, J. R. *Electrochem. Commun.* **2003**, *5*, 919.
- (33) Libao, C.; Xiaohua, X.; Jingying, X.; Ke, W.; Jun, Y. *J. Appl. Electrochem.* **2006**, *36*, 1099.
- (34) Croce, F.; Appetecchi, G. B.; Persi, L.; Scrosati, B. *Nature* **1998**, *394*, 456.
- (35) Yang, W.; Liu, X.; Qiao, R.; Olalde-Velasco, P.; Spear, J. D.; Roseguo, L.; Pepper, J. X.; Chuang, Y.-d.; Denlinger, J. D.; Hussain, Z. *J. Electron Spectrosc. Relat. Phenom.* **2013**, DOI: 10.1016/j.elspec.2013.03.008.
- (36) de Groot, F.; Kotani, A. *Core Level Spectroscopy of Solids*; CRC Press Taylor & Francis Group: Boca Raton, FL, 2008.
- (37) Bansal, R. C.; Bhowmick, A. K.; Custodero, E.; Donnet, J.-B.; Funt, J. M.; Gerspacher, M.; Herd, C. R.; Hess, W. M.; Julien, P. C.; Kuhner, G.; Mechaute, A. L.; Probst, N.; Rivin, D.; Sifleet, W. L.; Tomme, M.; Tricot, C.; Voll, M.; Wang, M.-J.; Wolff, S. *Carbon Black*, 2nd ed.; Marcel Dekker, Inc.: New York, 1993.
- (38) Jow, T. R.; Shacklette, L. W. *J. Electrochem. Soc.* **1988**, *135*, 541.
- (39) Pei, Q. B.; Yang, Y. *J. Am. Chem. Soc.* **1996**, *118*, 7416.
- (40) Liu, W. R.; Yang, M. H.; Wu, H. C.; Chiao, S. M.; Wu, N. L. *Electrochem. Solid State* **2005**, *8*, A100.
- (41) Lee, J.-H.; Paik, U.; Hackley, V. A.; Choi, Y.-M. *J. Power Sources* **2006**, *161*, 612.
- (42) Park, H.-K.; Kong, B.-S.; Oh, E.-S. *Electrochem. Commun.* **2011**, *13*, 1051.
- (43) Magasinski, A.; Zdyrko, B.; Kovalenko, I.; Hertzberg, B.; Burtovyy, R.; Huebner, C. F.; Fuller, T. F.; Luzinov, I.; Yushin, G. *ACS Appl. Mater. Interfaces* **2010**, *2*, 3004.
- (44) DeLuca, C. M.; Maute, K.; Dunn, M. L. *J. Power Sources* **2011**, *196*, 9672.
- (45) Hu, X. D.; Jenkins, S. E.; Min, B. G.; Polk, M. B.; Kumar, S. *Macromol. Mater. Eng.* **2003**, *288*, 823.
- (46) Liu, G.; Baker, G. L. *Soft Matter* **2008**, *4*, 1094.
- (47) Li, X. D.; Bhushan, B. *Mater. Charact.* **2002**, *48*, 11.
- (48) Jardret, V.; Zahouani, H.; Loubet, J. L.; Mathia, T. G. *Wear* **1998**, *218*, 8.

- (49) Gao, B.; Kim, J. K.; Leung, C. K. Y. *Compos. Sci. Technol.* **2004**, *64*, 2557.
- (50) Owens, J. F. P.; Lee-Sullivan, P. *Int. J. Adhes. Adhes.* **2000**, *20*, 47.
- (51) Kresse, G.; Furthmüller, J. *Phys. Rev. B* **1996**, *54*, 11169.
- (52) Blochl, P. E. *Phys. Rev. B* **1994**, *50*, 17953.

# Supporting Information

## Toward an Ideal Polymer Binder Design for High-Capacity Battery Anodes

Mingyan Wu,<sup>1</sup> Xingcheng Xiao,<sup>2</sup> Nenad Vukmirovic,<sup>3</sup> Shidi Xun,<sup>1</sup> Prodip K. Das,<sup>1</sup> Xiangyun Song,<sup>1</sup> Paul Olalde-Velasco,<sup>4</sup> Dongdong Wang,<sup>1</sup> Adam Z. Weber,<sup>1</sup> Lin-Wang Wang,<sup>5</sup> Vincent S. Battaglia,<sup>1</sup> Wanli Yang,<sup>4,\*</sup> and Gao Liu,<sup>1,\*</sup>

<sup>1</sup>Environmental Energy Technologies Division, Lawrence Berkeley National Laboratory, Berkeley, CA 94720, USA

<sup>2</sup>General Motors Global Research & Development Center, 30500 Mound Road, Warren MI 48090, USA

<sup>3</sup>Scientific Computing Laboratory, Institute of Physics Belgrade, University of Belgrade, Pregrevica 118, 11080 Belgrade, Serbia

<sup>4</sup>Advanced Light Source, Lawrence Berkeley National Laboratory, Berkeley, CA 94720, USA

<sup>5</sup>Materials Sciences Division, Lawrence Berkeley National Laboratory, Berkeley, CA 94720, USA

\*Corresponding authors: wlyang@lbl.gov; gliu@lbl.gov

Supplementary Contents:

Supplementary Methods (Page S2-S3)

Supplementary Figures S1-S8(Page S4-S11)

## Supplementary Methods

**Electrode Surface Plasma Treatments** Plasma etching treatment of electrode surfaces was carried out with Plasma-Thermal Parallel Plate Plasma Etcher (Plasma-Therm PK-12 RIE) using argon (Ar) gases as sources. The etching treatment condition in this study was using power at 250 watts (W) and Ar flow rate at 100 sccm for 30 minutes.

**Binder Swelling Test** The compatibility of the binder with the electrolyte solvent was examined by the swelling test. Binder sheets were prepared by solution-cast samples and the solvents were removed under vacuum oven at 80 °C. Binder sheets were then placed in ethylene carbonate (EC) and diethylene carbonate (DEC) (1:1 w/w) at room temperature. Weight measurements were made by blotting the samples dry and immediately weighting them. The swelling ratio was defined as the weight ratio of the amount of solvent absorbed to the dry weight of the tested binder sheet.

**Electron Microscopy** Composite electrode surface images were collected with a Hitachi S-4300SE/N scanning electron microscope (SEM) with an accelerating voltage of 15 kilovolts (kV) using the high vacuum mode at room temperature. High-resolution transmission electron microscope (HRTEM) images were obtained on a Philips CM200 field emission microscope operated at 200 kV at the National Center for Electron Microscopy (NCEM) at Lawrence Berkeley National Laboratory (LBNL).

**Adhesion Test** Adhesion measurements of the Si electrode were performed on a Chatillon® TCD225 series force measurement system. The Cu side of the Si electrode (1.2 cm × 1.2 cm) was fixed vertically to the bottom sample holder. The adhesive side of a 3M Scotch Magic® tape was applied onto the electrode laminate side firmly. The peel track was 1.2 cm wide. The Scotch Magic tape was peeled using the top sample holder at the direction of 180° angle to the adhered tape and parallel to one side of the Si electrode. The peeling speed was fixed at 7" min<sup>-1</sup> moving rate to the bottom sample holder. The force applied to the adhered tape was recorded during the peeling process. When the tension was fully applied and the electrode laminate was peeled off, the measured force value reaches a plateau, representing the adhesion force of the electrode laminates. As shown in Fig.S5, PFM based electrode exhibit such plateau in peel test data. However, the adhesion force of PEFM is stronger than the measurement range of such method, so no clear plateau is displayed, and the whole electrode remains on the Cu current collector. Such peel test is a standard measurement of adhesion force in battery industry, the results in Fig. S4 indicates the unusually high adhesion force of the developed PEFM polymer binder.

**Contact Angle Measurements** Experimental measurements of contact angles were performed with a custom-made automated goniometer (ramé-hart Model 590), which is capable of two-way injection and two-way image capturing. The system is displayed in Supplementary Fig. S8. A charge-coupled device (CCD) camera (70 feet per second [fps]) of 640 × 480 pixels is utilized to capture images every quarter second, with a 150 W halogen lamp used as a backlight. The sample was first placed on the sample stage on

top of a double-sided tape to avoid any displacement. A fixed volume of liquid water was then injected from above by a needle using an automated dispensing system with a constant injection rate. The sample-stage slowly raised until contact with the drop and slowly lowered as the drop was formed, to minimize any kinetic impact from the drop falling to the sample surface, which could produce erroneous measurements and add variability to the system. The optimum injection rate was determined using several measurements. For smaller drops, it was found that the contact-angle data were statistically consistent for the injection rate of 2 microliters per second ( $\mu\text{L/s}$ ) or slower. However, in this study, we used a fixed drop volume of 10  $\mu\text{L}$  and an injection speed of 0.5  $\mu\text{L/s}$  for better accuracy. Movement of the stage was vibration-free, with no backlash, and vibrations from the surroundings were isolated from the stage using an anti-vibration stage. Several measurements were taken for each sample, while three contact-angle measurements were taken for each droplet with 1-second time interval using DROPimage<sup>®</sup> software.

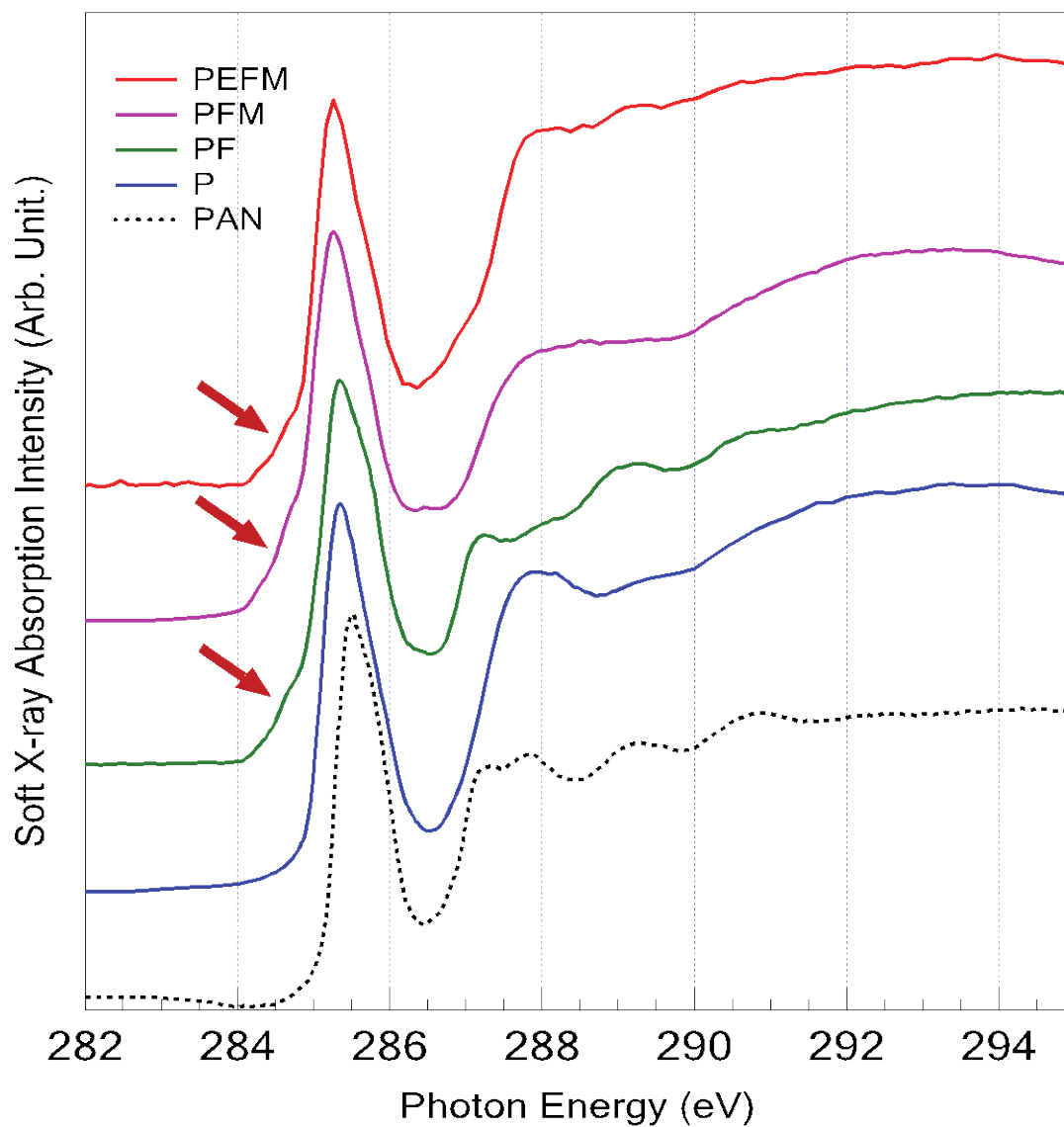


**Figure S1.** Full spectra of soft x-ray C-K XAS of a series of conductive polymers. Conventional polyaniline (PAN) is also plotted for comparison purpose. It is clear that all polymer materials with fluorenone (F) group exhibit the low energy shoulder, corresponding to a much lower energy of their LUMO levels. Incorporating E and M portions in PFM and PEFM only affect the high-energy features above 287 eV, without disturbing the critical electron LUMO states indicated by red arrows.

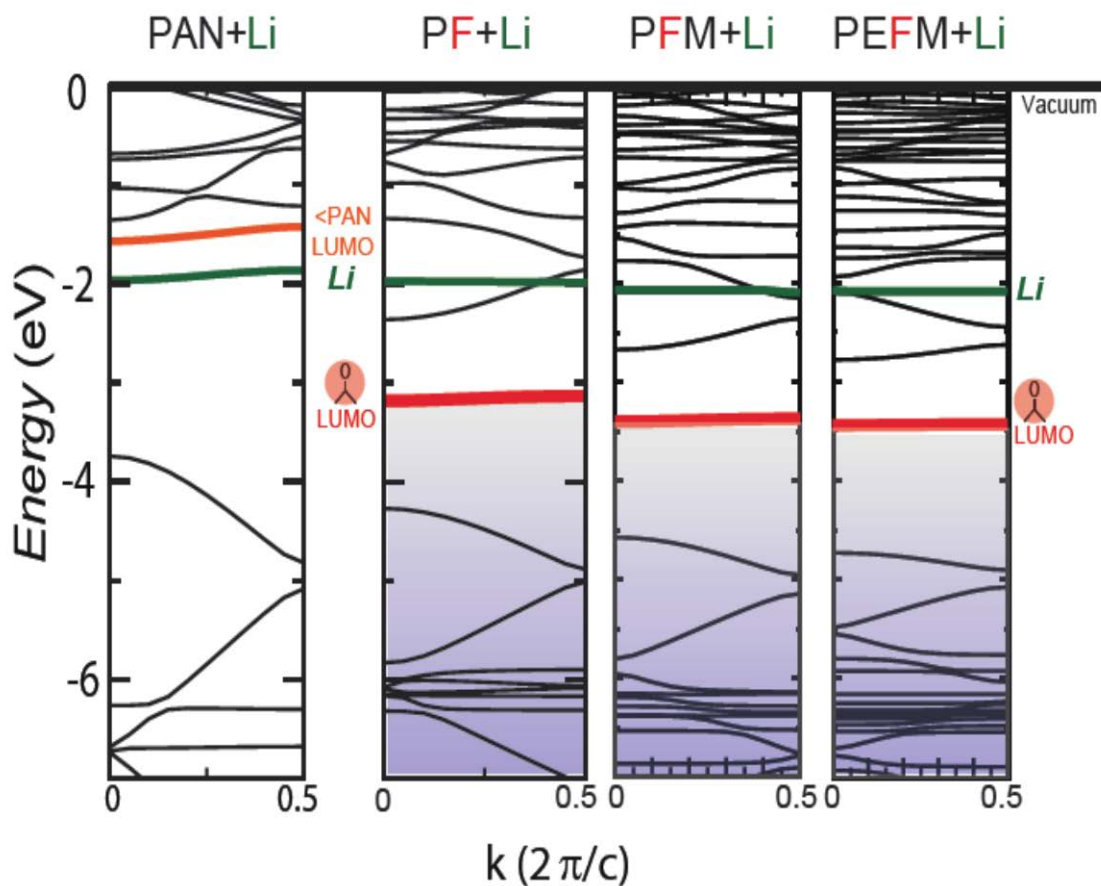


**Figure S2.** DFT calculations of the band structure of a series of conductive polymers with lithium attached. Li-induced bands are marked as green. While conventional PAN polymer shows higher LUMO level (orange) than Li-induced band, all polymer with fluorenone (F) group exhibit lower LUMO levels (red) comparing with Li-induced bands. In the battery chemistry, Li will thus introduce *in-situ* electron doping to the low energy LUMO states in polymers with F groups. The details for PF polymer has discussed intensively in Ref [28].

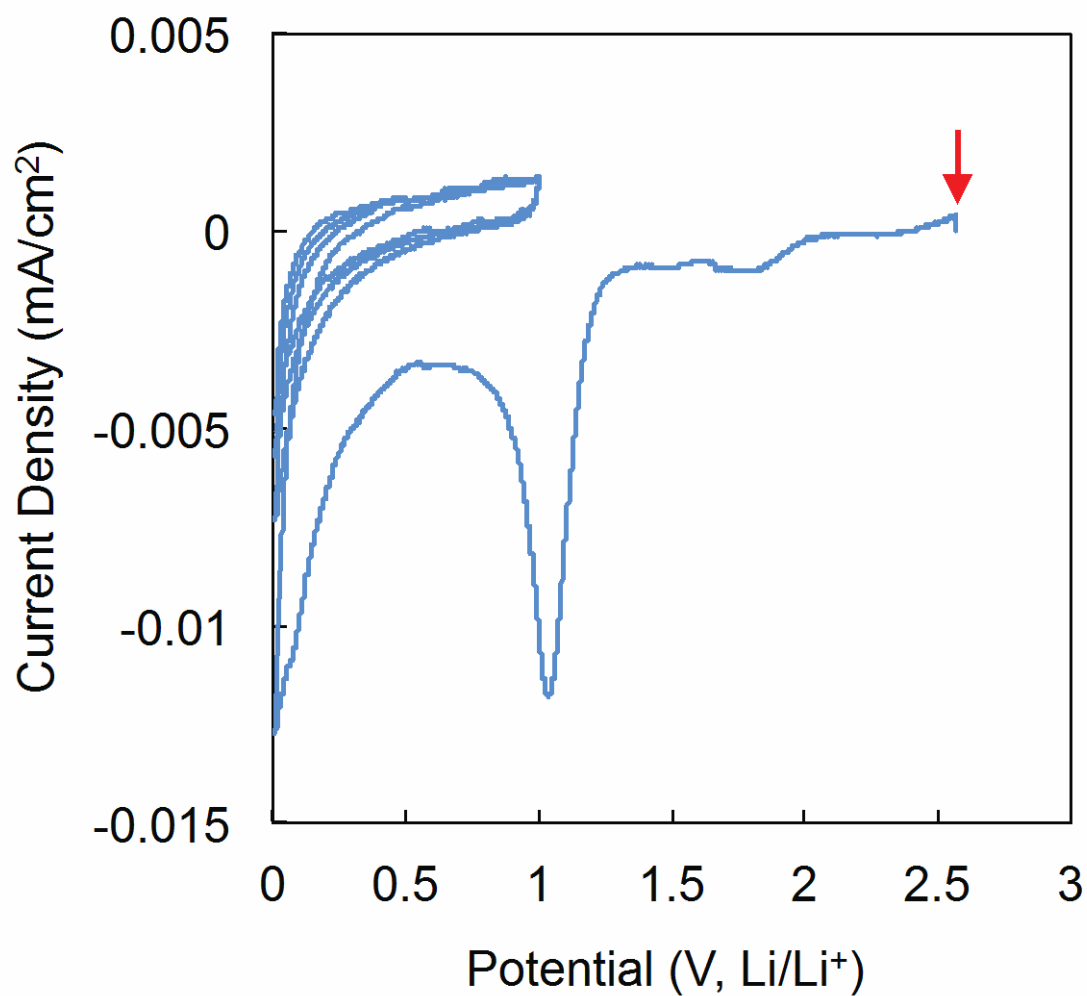


**Figure S3.** Circular voltammetry of pure PEFM conductive polymer binder film at 0.2 mV/s scan rate. There is irreversible Li doping around 1.1 V Li/Li<sup>+</sup> at the first lithiation step. The red arrow points to the initial state.

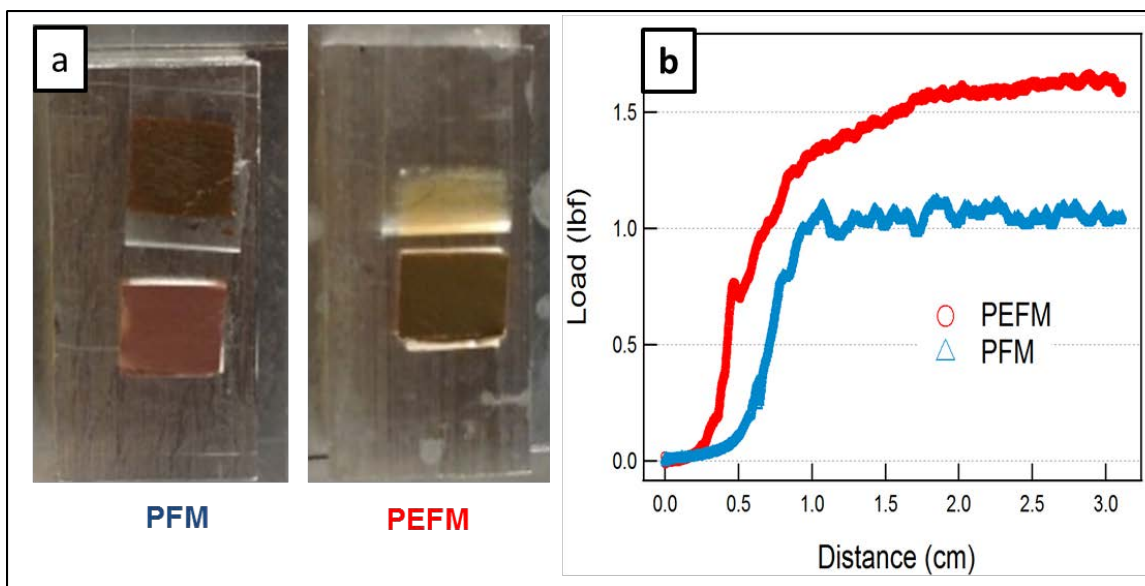


**Figure S4.** Peel tests comparison of the electrode laminate made with PFM and FEFM binder. (a) Peel testing photos of the two electrodes during the tests. The photo shows the PFM based electrode was peeled off (left), but PEFM based electrode remains attached to the Cu current collector with only small amount of surface materials peeled off by the tape (right). This shows that the adhesion force of the developed PEFM is too strong to be measured by such conventional method. (b) Force measured during the peel tests of PFM and PEFM based electrodes. Note again that the adhesion force of PEFM based electrode is beyond the measurement range of such method, and actually even higher than the value (1.7 lbf) showed by the red curve.

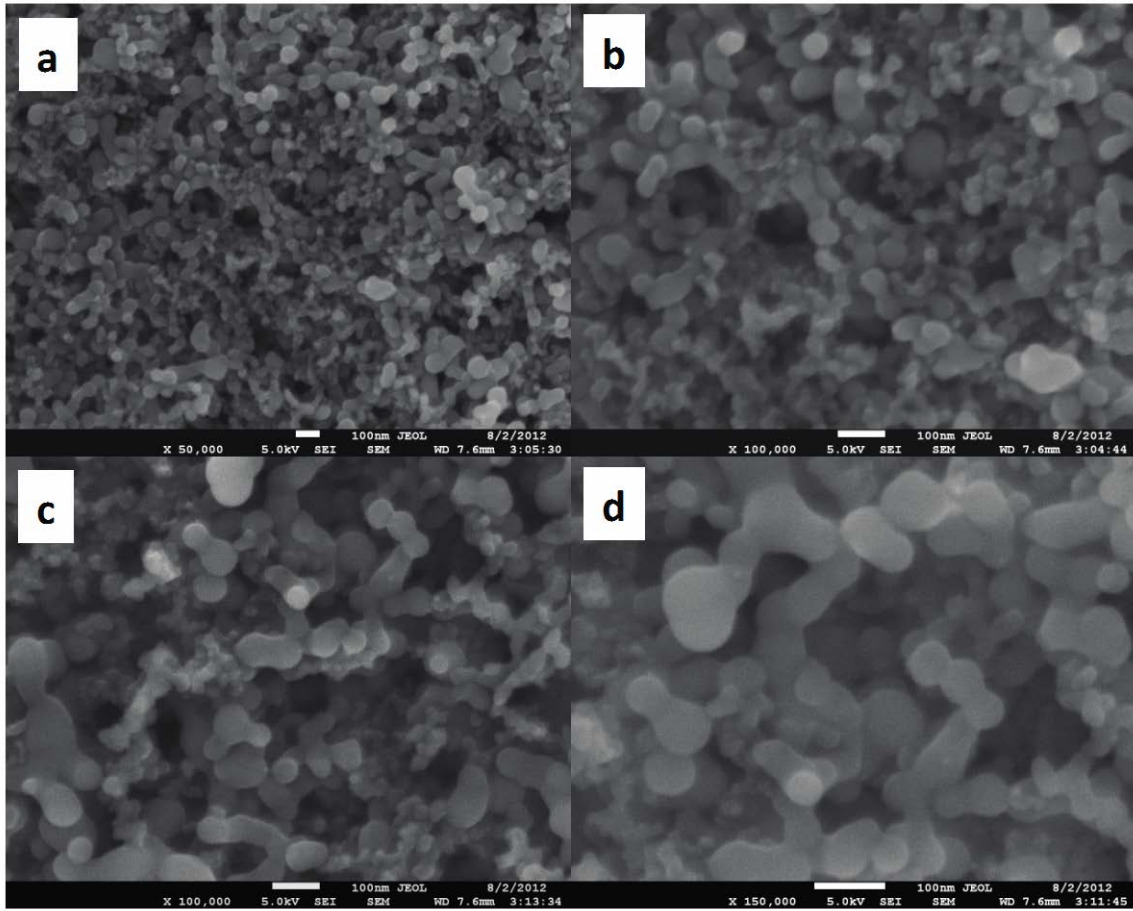


**Figure S5.** SEM surface images of the Si/PEFM composite electrode at different magnification levels. Magnification increases from (a) to (d). White bars show 100 nm scale in each image.

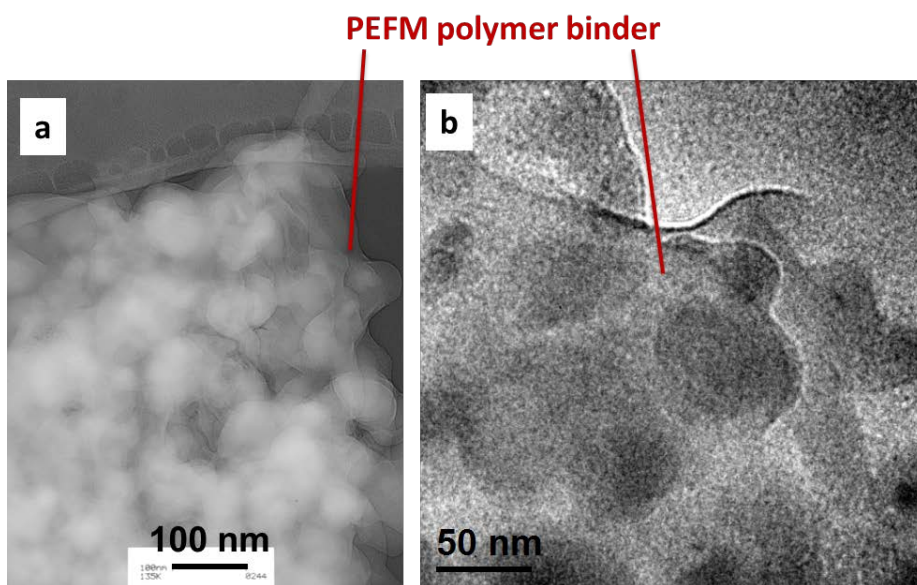


**Figure S6.** TEM images of the Si/PEFM electrode after 1 full lithiation and delithiation cycle. Electron diffraction in Fig.5 is taken on the entire area of (a) here.

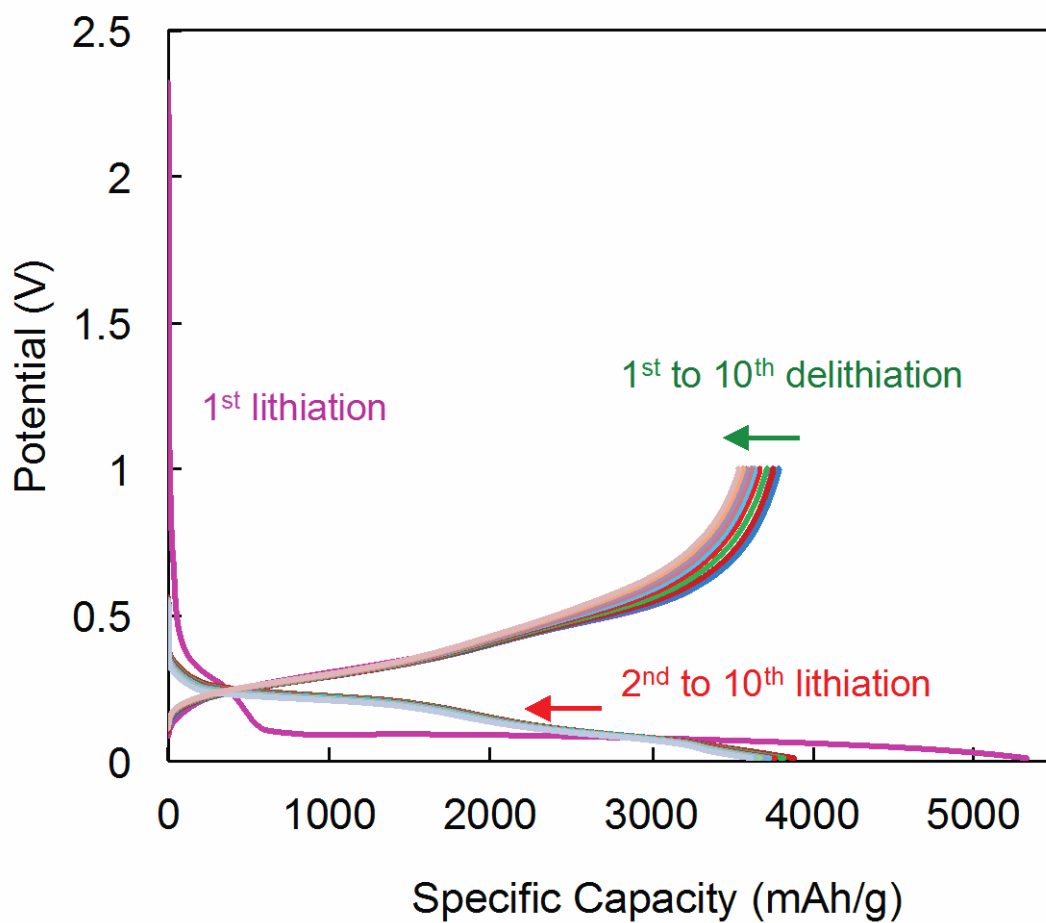


**Figure S7.** The initial lithiation and delithiation of Si/PEFM electrode in the first 10 cycles at C/10 rate. The arrows show the direction of sequence of lithiation and delithiation.

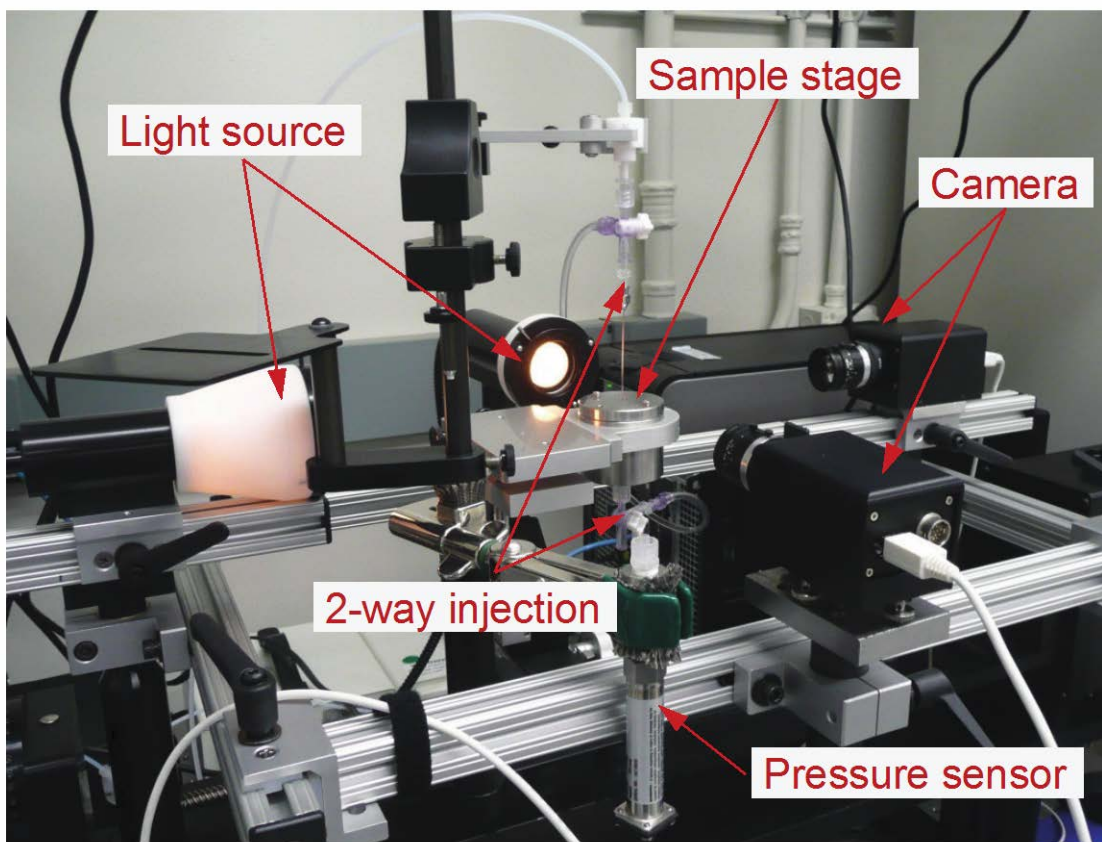


**Figure S8.** Experimental setup of goniometer for measuring contact angles of water (Fig.4a) on the conductive polymer binders' surface.